IOP Conf. Series: Materials Science and Engineering **219** (2017) 012001 doi:10.1088/1757-899X/219/1/012001

Degradation of metallic materials studied by correlative tomography

T L Burnett[1]*, N J H Holroyd[2], J J Lewandowski[2], M Ogurreck[3], C Rau[3], R Kelley[4], E J Pickering[1], M Daly[1], A H Sherry[4], S Pawar[1], T J A Slater[1], P J Withers[1]

[1]School of Materials, The University of Manchester, Oxford Road, Manchester, M13 9PL, UK
[2]Department of Materials Science and Engineering, Case Western Reserve University, Cleveland, OH, USA
[3]Diamond Light Source, Harwell Science and Innovation Campus, Fermi Ave, Didcot OX11 0DE
[4]Thermo Fisher (previously FEI Company), 5350 NE Dawson Creek Drive, Hillsboro, OR 97124, USA
[5]National Nuclear Laboratory, Chadwick House, Birchwood Park, Warrington, WA3 6AE, UK

*timothy.burnett@manchester.ac.uk

Abstract. There are a huge array of characterization techniques available today and increasingly powerful computing resources allowing for the effective analysis and modelling of large datasets. However, each experimental and modelling tool only spans limited time and length scales. Correlative tomography can be thought of as the extension of correlative microscopy into three dimensions connecting different techniques, each providing different types of information, or covering different time or length scales. Here the focus is on the linking of time lapse X-ray computed tomography (CT) and serial section electron tomography using the focussed ion beam (FIB)-scanning electron microscope to study the degradation of metals. Correlative tomography can provide new levels of detail by delivering a multiscale 3D picture of key regions of interest. Specifically, the Xe^+ Plasma FIB is used as an enabling tool for large-volume high-resolution serial sectioning of materials, and also as a tool for preparation of microscale test samples and samples for nanoscale X-ray CT imaging. The exemplars presented illustrate general aspects relating to correlative workflows, as well as to the time-lapse characterisation of metal microstructures during various failure mechanisms, including ductile fracture of steel and the corrosion of aluminium and magnesium alloys. Correlative tomography is already providing significant insights into materials behaviour, linking together information from different instruments across different scales. Multiscale and multifaceted work flows will become increasingly routine, providing a feed into multiscale materials models as well as illuminating other areas, particularly where hierarchical structures are of interest.

1. Introduction to correlative tomography

In this paper correlative tomography [1] will be introduced and in particular how plasma focused ion beam microscopy (PFIB) [2] has been used to extend this.

Much can be learnt from observations of metallographic sections, to better understand many metal systems. However 3D characterization is also sometimes required, for example to understand complex interfaces, porous networks and phase distributions. Fortunately, there are an increasing number of powerful characterisation techniques available, for example, X-ray computed tomography (CT) [3], serial section tomography (SST) using either optical or electron imaging [4-5], transmission electron tomography [6], and atom probe tomography [7], with each covering different length scales.

Traditionally, data collected at different scales are not spatially correlated. Instead, features at the different scales are captured by various different techniques in parallel on different samples and the data brought together where necessary in a statistical manner. This approach is limited when the observed behaviour is rare or relies on extremes, for example the initiation and growth of fatigue cracks. In such cases it is sometimes highly desirable to track the evolution of specific sites (e.g. locations where microcracks begin to form) and to study these unusual features and understand their behaviour across a range of length scales. In many cases, including the fatigue example, the process evolves over time to cover different length scales. For example, a fatigue crack may initiate due to a persistent slip band in a single grain of a metal microstructure at the surface of a specimen, the crack then starts to form and starts to propagate across the grains and soon will cover many grains. Final failure will typically occur once the fatigue crack reaches a critical length and there is fast catastrophic failure of the entire sample or component. As such the key length scales evolve from microns (e.g. a single grain or smaller), to hundreds of microns (e.g. multiple grains), to the tens of centimetre (entire component) scale. Moreover, with each different length scale there is also a different timescale that should be used to effectively observe the process.

Figure 1 illustrates a multiscale and multi-instrument scheme. The collection of chemical information as well as morphological information also provides a multi-faceted picture of the sample. The example shows a sample imaged in 3D non-destructively (e.g. by X-ray CT) under a mechanical or environmental load (1). A region of interest (RoI) is identified from this sample and this sub-region is prepared for subsequent imaging (2), which could be laser machining or electro-discharge machining (EDM) out the RoI, for example. The sample is then ready to be imaged destructively in 3D (3). Several higher resolution 3D imaging techniques rely on the scanning electron microscope (SEM), for imaging but use different methods of slicing to prepare the serial sections, for example, mechanical polishing [8], broad ion beam milling [9], and focussed ion beam milling [10], or ultramicrotomy for softer materials [11]. During this high resolution 3D imaging a further region of interest is identified, which could, for example, be a buried inclusion or the tip of a crack or a particular grain boundary. A sample including the region of interest is then prepared (4) at this scale usually by FIB machining, but possibly also by etching/electropolishing/microtomy, although site specific targeting is more difficult with these latter techniques. Lastly, the nanoscale chemistry and morphology of this region of the sample could be characterized (5), for example by atom probe tomography or STEM-EDS tomography.

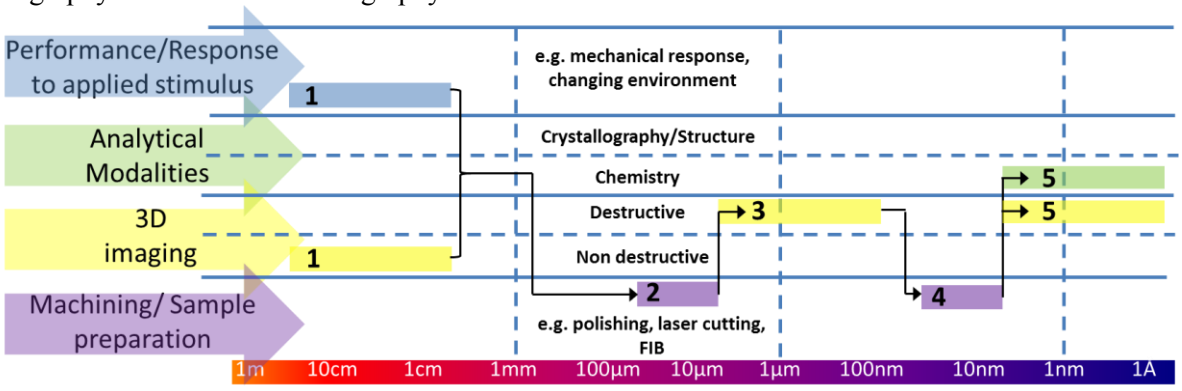

Figure 1. Diagram showing a workflow for a multiscale materials analysis. The horizontal axis is lengthscale and the large coloured arrows show different aspects related to understanding material

properties. The workflow, connected by the black arrows, gives an example combination of techniques and scales.

It is becoming increasingly important to be able to efficiently carry out such workflows in order to build up information for multiscale models or to identify the critical length scales that govern a damage mechanism. It is the ability to effectively couple existing and highly specialized pieces of equipment to follow the same RoI, often with demanding sample requirements, that will allow the fullest exploitation of the currently available technology. There are several major benefits to this approach, such as being able to find rare regions of interest through coarse scanning for subsequent detailed analysis and also by providing context and proof of the representativeness of a minute region chosen for more detailed analysis. One of the major challenges is that many instruments and techniques have been refined and developed regardless of whether this makes it more difficult to effectively link it to other techniques. There is also benefit in targeting specific areas for detailed analysis relating to managing the data generated. Without proper targeting it is easy to collect very detailed information for large volumes and create unwieldy datasets which are costly and time-consuming to analyse. If it is possible to positively identify smaller regions which require the detailed analysis, this not only limits the quantity of data collected it may also be more practical to collect further facets of information, for example the chemistry, crystallography, mechanical response etc. which would be practically prohibitive for larger volumes at high resolution.

The correlative aspect of such workflows comes in two ways: coordinate-correlated, and feature-correlated. Coordinate-correlated volumes use dimensional measurements to provide the spatial registry through a coordinate system, for example the coordinates of the sample stage in the microscope. Alternatively it is possible to register to sub-volumes by identifying specific features common to both the original data volume and the sub-volume. However in order for a method to be correlative it is necessary to be able to register the sample features from one level to another. The resolution of the two techniques means that the same features can be seen in both images and confidently registered with complementary information coming from both results [12-14]. Multiple layers of different information can be built up and correlated based on common features between many different techniques e.g. within the AFM [15].

In this paper a number of characterization approaches will be presented. Each of these will be discussed individually but then also with respect to integration into more extensive correlative tomography workflows.

2. Time-lapse imaging by X-ray CT

Time-lapse imaging using X-ray CT, also sometimes loosely referred to as 4D imaging, is an extremely powerful way of understanding behaviour and performance, as it is possible to observe the evolution of the phenomena [16]. It is often not possible to identify post-mortem the sequence of events that has led to the final condition of the specimen. As such, time-lapse imaging can be invaluable, however it is often experimentally challenging, creates enormous amounts of data and may demand the use of national facilities such as synchrotron sources, which can lead to high costs and/or long lead times. The big-data challenge is particularly formidable as detailed post-processing and analysis is often required to make sense of this data.

Time-lapse imaging has been used to investigate many processes including fatigue in metals and composites [17-18], ductile fracture [19], corrosion [20], battery performance [21], geological processes [22] and even insect life-cycles [23] and flight [24]. It is possible to push the temporal resolution to exceptionally fast times, down to <<1 second, for a full tomogram [3], but equally, long duration experiments are possible, with samples imaged once every few days or weeks so that long duration processes may also be observed. The intention in each case to observe the phenomena at realistic time scales. This leads to one of the major considerations in carrying out time-lapse experiments, that of matching the timescales of the process to the requirements of the imaging.

Taking the example of a growing corrosion pit and the fact that the pit takes 12 hours to grow to full size of 100 μm across (the appearance of the pit is a hemispherical surface cavity, with a diameter

of 100 μm), then assuming a constant growth rate we would expect a growth of just over 8 μm per hour. From ex situ experimentation it was discovered that during the total growth there are periods of faster and slower growth such that it is estimated the growth rate fluctuates between 4 and 12 μm growth per hour. Here the growth rate determines the time within which a tomography scan must be recorded. For example, it is clear that if the 3D imaging takes 6 hours, only one tomogram can be recorded within the growth period of the pit. Furthermore, as the pit will have grown significantly in the time between the first projection and the last the image will be blurred, leading to poor quality data. The spatial resolution of the imaging is also intimately linked to the temporal resolution. Taking the average growth rate of 8 μm/h and assuming one tomogram takes 1 hour to record, this will only be worthwhile if the spatial resolution is better than 8 μm in order to resolve the changes. This is a careful balance however as too high resolution would again lead to blurring in the reconstructed images as small changes are occurring during the collection of the raw projection data. Another consideration is the field of view, which must be sufficient to capture the features of interest at the start and finish of the time period where the sample is observed. This may not be the case if the resolution is too high (current detectors mean that the field of view is generally ~1000x the spatial resolution [3]).

2.1 Exemplar: environmentally induced cracking of AA5083-H131 aluminium alloy

In this exemplar the environmentally induced cracking of a 5xxx alloy is investigated. Ex-situ analysis via X-ray CT had revealed a previously un-reported mode of environmentally assisted fracture [25]. Time-lapse X-ray CT was carried out to observe the crack propagation in situ to help elucidate the nature of propagation and mechanisms of this fracture mode. In this exemplar mm-sized specimens are investigated with microscale resolution with a temporal resolution of the order of minutes.

Round bar tensile specimens of 3.2 mm diameter and 12.7 mm gauge length were prepared from a 29 mm thick rolled plate of Al-Mg-Mn alloy, AA5083-H131, in the short transverse direction. The alloy had a typical ‘pancake-like’ grain structure with a grain size of 150 μm (L), 80 μm (LT), and 35 μm (ST) directions respectively [26].

The samples were then sensitized at 80 °C for 250 hours to create a susceptible microstructure. Following sensitization, the tensile samples were soaked in a 0.6M NaCl solution for 250 hours. This achieved two things: 1) The creation of sites of intergranular corrosion on the sample surface, and 2) charging of the samples with hydrogen. The experiment is described in further detail by Holroyd et al [25].

Immediately following the sensitization/pre-exposure treatments, the tensile specimens were subjected to slow strain rate testing (SSRT), typically employing a nominal strain rate of ~10^{-5} /s, while being exposed to humid laboratory air (relative humidity, 50%).

The sample was interrupted just before the final failure. This ‘intact’ but heavily cracked sample was then analyzed using a Zeiss Xradia Versa 520 X-ray CT system operating at 70 kV and using the 4x coupled optical magnification and an exposure time of 30 s and 2001 projections, providing a voxel size of $(1.7\ \mu m)^3$. The time-lapse data were collected on samples prepared in the same way and tested under the same conditions, but this time on the I13 imaging beamline at Diamond Light Source. A pink beam was used to maximize flux around a nominal energy of 35 keV. The detector provided a 4.5 x 5.6 mm field of view with a 2.6 μm voxel size. The exposure time was 200 ms for each of the 1200 projections. The tensile testing was conducted using a Deben CT5000 in-situ rig with local sample containment creating high local humidity.

Figure 2 shows multiple views of the tested and interrupted test specimens. The virtual slices (figure 2b) and 3D rendering of the cracking in the sample (figures 2c, d and e) show the morphology of the environmentally induced cracks that resulted. As shown in figure 3(a), and in comparison to figure 2, it is possible to see three different stages of crack propagation. The first stage is intergranular corrosion (IGC). These sites are formed in the pre-exposure step and act as stress raisers to initiate the ‘Type 1’ cracking, which is intergranular stress corrosion cracking (IGSCC). Type 1 cracking is characterized by its very flat, smooth and direct morphology. After a period of propagation of the

Type 1 crack the cracking changes to Type 2 cracking. Type 2 cracking is easily identified from the virtual slices of the X-ray CT data as being highly topographical, composed of steps linked by almost vertical tears. This mode of fracture has previously been overlooked and is often difficult to see from the fracture surface, partly due to the great depth of field in the scanning electron microscope not highlighting the topographical changes in the fracture surface. If taken to failure there is also a final fast fracture region consisting of a 45° shear lip.

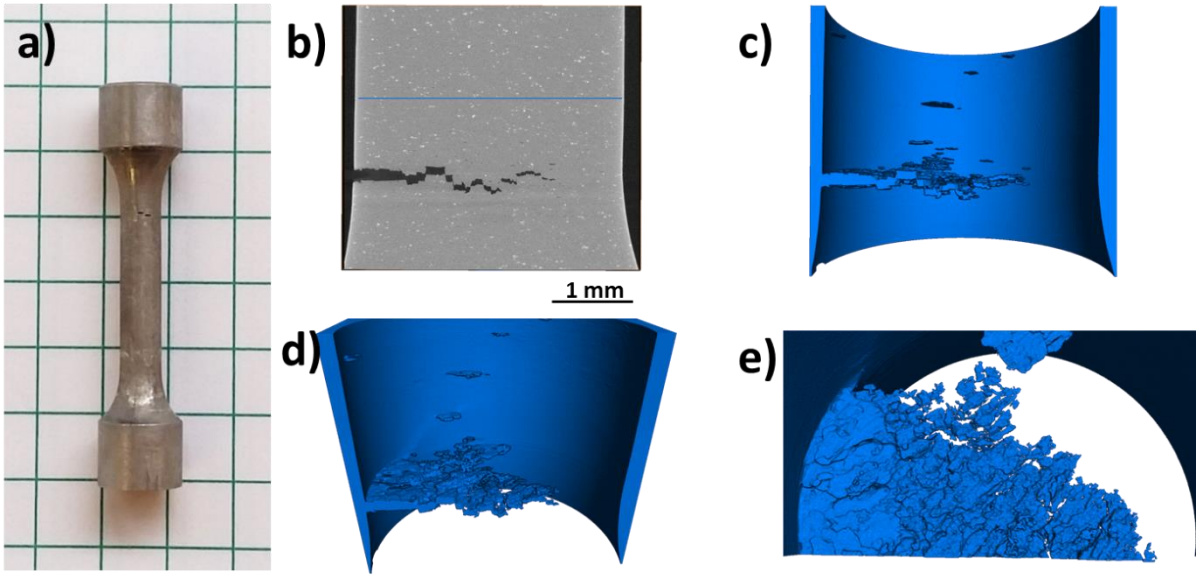

Figure 2 a) A photograph of the 3.2 mm diameter AA5083-H131 round bar tensile specimen prepared in the short transverse direction. b) virtual slice of the reconstructed X-ray CT data showing the large crack. c), d) and e) Volume Renderings of the crack shown from different directions with the crack visualized as if it were solid and the metal rendered transparent.

The other curious feature of the Type 2 cracking is the fact that surrounding this crack region there are multiple regions of isolated internal damage (figure 3a). Such regions do not occur around the Type 1 crack. The regions are associated with second phase particles (see black arrows). This observation, coupled with the knowledge of the mechanical characteristics of the failure, has led to a proposed mechanism for the propagation of the Type 2 cracking illustrated in figure 3(b). The diagram shows how the process zone ahead of the crack tip creates damage in the material which is isolated. These isolated regions of damage are then linked through regions of microvoid coalescence and the crack jumps forward. The crack halts as damage has not formed further ahead than the process zone and as such the crack arrests when there is sufficient intervening metal, i.e., no route to link isolated damage regions. The sample ‘re-loads’ and the isolated damage is formed ahead of the new crack tip position before the next jump. This mechanism was proposed by Holroyd et al [26] from ex-situ observations of X-ray CT and SEM fractography data.

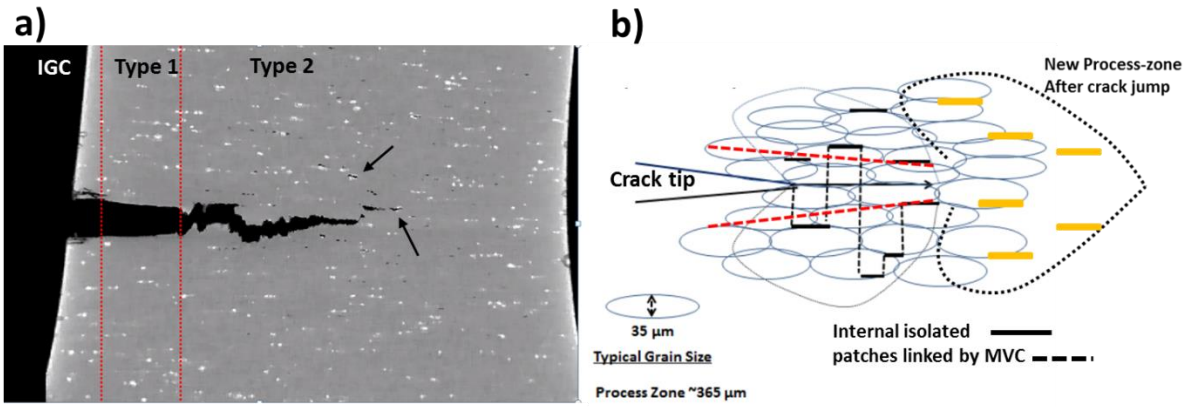

Figure 3 a) Virtual slice of the reconstructed data showing in detail the different stages of cracking and also regions of isolated damage (black arrows) ahead of the Type 2 crack. b) Diagram detailing the proposed mechanism of propagation for the Type 2 cracking.

Figure 4 shows results from the time-lapse data recorded at I13 Diamond Light Source. The data is taken from a sample tested under the same conditions and shows two examples of two different locations, where a crack tip can be seen, as well as a region of isolated damage ahead of the crack tip (time=t_1). Four minutes elapsed during the collection of the 3D tomograms, of which these are virtual slices, and in that time the crack can be seen to have linked to the isolated regions via a near-vertical steps. Once at the new position at time=$t_{1+4mins}$ new regions of isolated damage have formed ahead of the crack tip. The regions ahead of the crack shown here were confirmed to be isolated looking through multiple slices around these regions. It has been confirmed that the crack propagation stops and starts and that the crack tip only has influence a limited distance ahead of it. This confirms the theory proposed from *ex situ* testing and adds clarity to the process for this newly reported mode of environmentally induced cracking. A number of further questions have also been raised such as whether the sudden spurt in growth, also associated with a jump in crack opening displacement, leads to blunting of the crack tip.

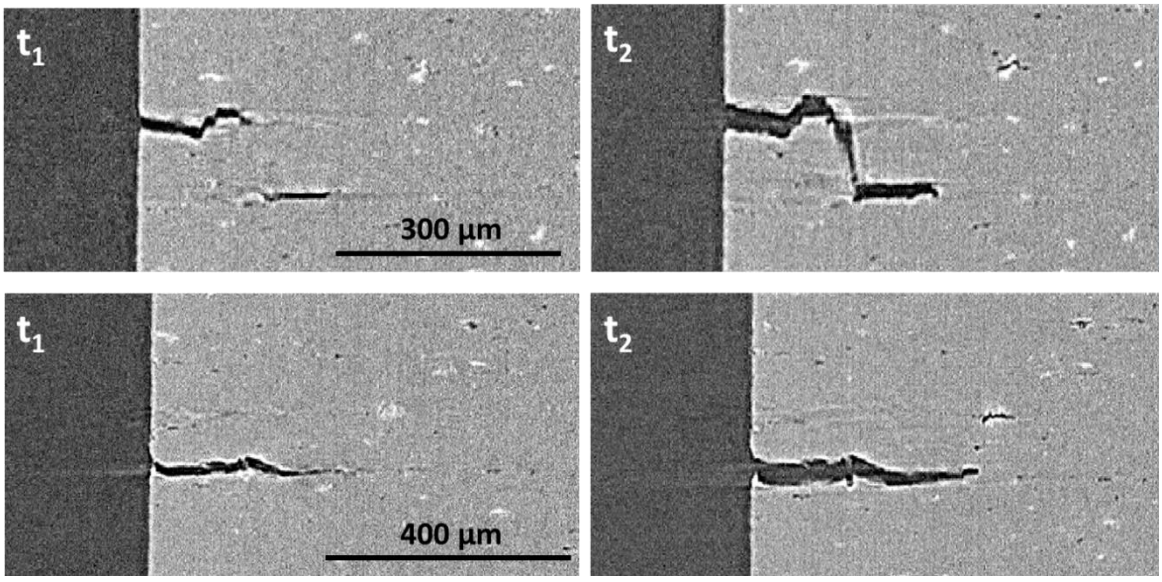

Figure 4. Two examples of virtual slices from the same sample of the reconstructed synchrotron CT data of the same position at two different time steps, t_1 and $t_{1+4mins}$. The crack tip progresses and when at the new position new regions of isolated damage ahead of the crack tip emerge which were not there previously.

3. Xe^+ ion plasma FIB: a tool for enabling multiscale analysis

Often there is the desire to investigate a specimen at multiple scales. In the example given in 2.1 it may still be desirable to investigate finer scale features, such as the grain boundary chemistry at the nanoscale. This may be an important aspect to in ultimately understanding the crack paths in the material. Recent work has shown how PFIB serial sectioning has been used for the collection of large, yet high resolution, and how datasets can be effectively used in conjunction with X-ray CT imaging (and indeed time-lapse X-ray CT) in a correlative manner [27].

The PFIB is an exciting tool that opens up the range of scales accessible with FIB technology in to the 100's of microns range whilst retaining the same nanoscale resolution [2, 28, 29]. In a 'traditional' Ga^+ FIB a volume of $(50\ \mu m)^3$ would be considered large, and whilst the milling of finer slices, down to ~10 nm thick, is possible, the practically achievable volume remains a limitation. Using a PFIB instrument volumes $(300\ \mu m)^3$ with 500 nm slice thickness have recently been demonstrated. It is also possible to combine the imaging of each slice with analytical data such as energy dispersive X-ray spectroscopy (EDS) and electron backscatter diffraction (EBSD). The desire to collect large 3D EBSD volumes is currently practically limited, with the bottleneck related to the EBSD map collection time, which typically accounts for 60-80% of the total time period for the completion of one 'slice' of data. However, recent developments in both the hardware [30] and software [31, 32] show great promise for limiting this bottleneck in the future. Whilst the nature of the damage is still being investigated, it appears that the Xe^+ is less damaging for equivalent milling parameters and, due to the inert nature of xenon, chemical incompatibility issues with elements such as Al and Cu are avoided.

3.1 Exemplar: ductile failure of SA508

In this example a volume of interest identified from X-ray CT data is analyzed in detail using serial sectioning tomography using the PFIB in order to understand the ductile failure mechanisms of a reactor pressure vessel SA508 Grade 3 steel. In this exemplar specimens are investigated from the cm-scale down the nanometer scale on a post-mortem basis.

The material investigated originated from a large SA508 Grade 3 [33] steel ring forging, in the quenched-and-tempered condition. Fracture toughness tests on the material were performed according to the European Structural Integrity Society (ESIS) P2-92 [34] standard, with tests performed on a sample of thickness B = 25 mm and width, W = 50mm using both the unloading compliance and the multi-specimen methods at room temperature. In order to probe the distribution of voids with depth using X-ray CT, cylindrical samples of ~0.5 mm diameter were prepared using electrical discharge machining (EDM) with the top of each sample incorporating the original fracture surface. A core was extracted from a region in the centre of the ductile fracture region ~2 mm ahead of the fatigue pre-crack.

X-ray CT was conducted using a Zeiss Xradia Versa 500 X-ray CT system. The voxel size was $(0.8\ \mu m)^3$ giving a resolution of 2-3 μm. The scan was performed at 100 kV, collecting 1,601 projections with an exposure time of 5 s per projection at 4x magnification. A FEI Helios PFIB was used for high-resolution investigations of the microstructure of the sample. A volume 150 x 115 x 18 μm in size was prepared with a slice thickness of 100 nm and a pixel size of 26 nm. Electron images were collected at 2 kV, 800 pA using the through-lens detector. The slices were milled using an accelerating voltage of 30 kV and current of 59 nA, providing the best balance of speed of milling and quality. Data analysis and visualization for all datasets was performed with the Avizo 9.0.0 software.

Figure 5a shows a surface rendering of the EDM core from the X-ray CT data, giving an appearance of the sample similar to that observed within the SEM. A sub-surface volume of interest was identified from the X-ray CT data including two voids of different geometries located ~600 μm below the fracture surface (see orange box in figure 5b)). The 3D rendering of the sample surface figure 5a) was used to relate the location of the voids (figure 5b)) to surface features, which were used as points of registration to plan the preparation of the volume for serial sectioning using the PFIB. The 3D rendering of the surface were directly compared to SEM images of the sample (see figure 5c)) and

features registered to enable the accurate machining of the specimen for serial sectioning analysis through the identified voids. Figure 5(d) shows the PFIB prepared sample with a block created ready for serial sectioning.

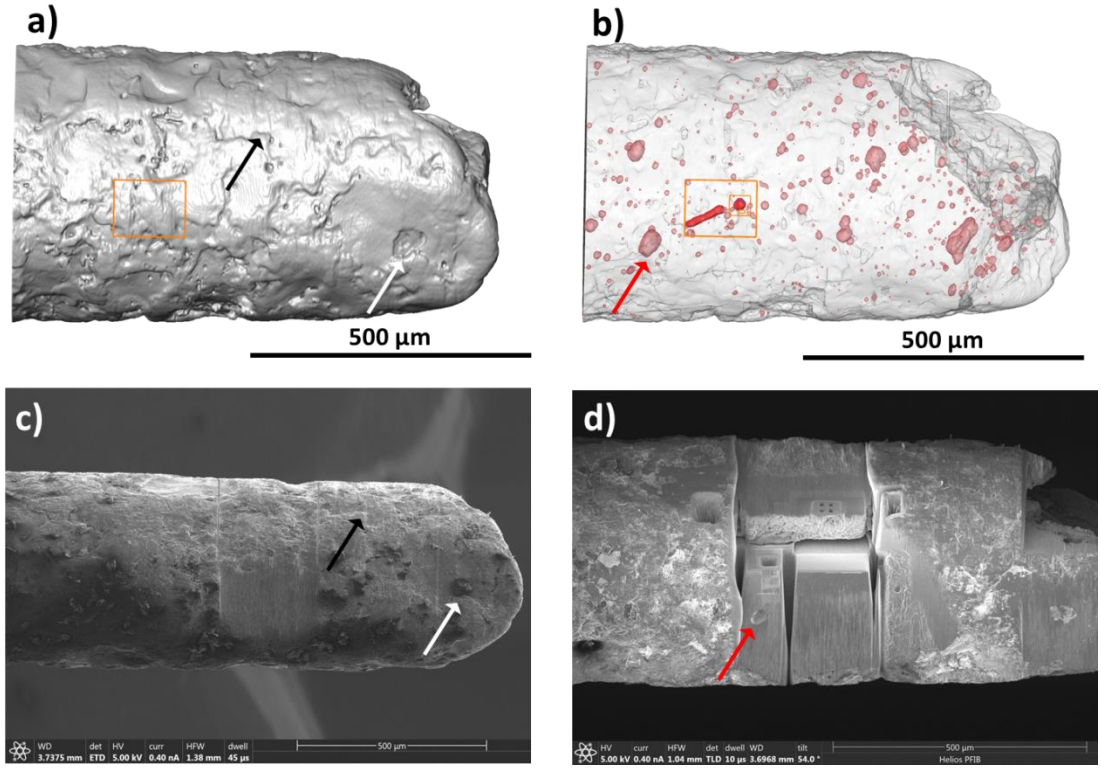

Figure 5 a) Volume Rendering of the reconstructed X-ray CT data showing the surface of the core specimen. The orange box shows the region of interest determined through comparison with b). The black and white arrows show two of the features used for registering the X-ray CT data to the SEM image of the sample shown in c). b) 3D rendering of the sample showing the internal voids. The orange box highlights two distinctive voids for further analysis. The red arrow shows another large void which can also be seen in the PFIB-prepared volumes in d) and used a reference point during machining. c) Secondary electron SEM image of the core, the contrast is dominated by some fine scale roughness but two feature used for correlation to the X-ray CT data in a) are shown with black and white arrows. d) Secondary electron image of the sample of preparation of the volume of interest for serial sectioning. The red arrow highlights a large void also visible in b) indicating the success of the correlation.

Figure 6(a) shows again the X-ray CT data highlighting the internal voids and the volume of interest. Figure 6(b) shows the region of interest as captured using the PFIB. The detailed microstructure of the steel is clear and the voids have been highlighted in red. Figure 6(d) shows the same region but this time with the inclusions captured highlighted in blue. Out of 9 of the voids captured within the PFIB sectioned volume 8 were associated with a manganese sulphide inclusion as determined by EDX (not shown). Figure 6(c) shows a magnified region of the PFIB data immediately adjacent to the large spherical void. This highlights the detail of the microstructure captured and shows an example of small voids that are associated with the carbides in the microstructure. These voids are associated with carbides and form close to the large voids and may be important in linking the large voids together in the final stages of fracture just prior to failure.

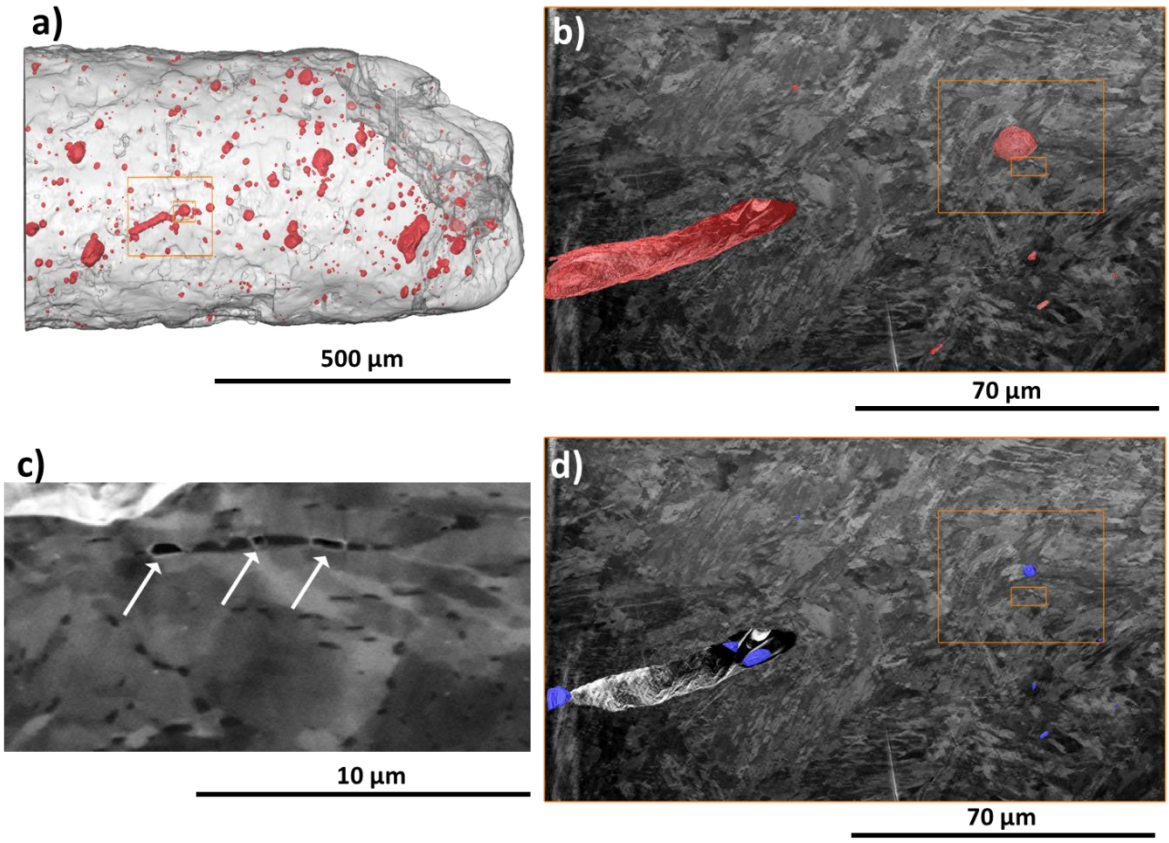

Figure 6 a) 3D rendering of the sample showing the internal voids. The orange box highlights two distinctive voids for further analysis using the PFIB. c) Though Lens Detector SEM image of one of the PFIB slices. Voids are highlighted in red, the two largest voids are also visible in a) but several other smaller voids are also visible. The large orange box highlights the large spherical void and the smaller orange box highlights the sub-region shown in c). c) shows a magnified region of b) showing the location of sub-micron voids (white arrows) associated with carbides which are found around the large voids. d) same as b) but highlighting in blue the inclusions associated with the voids.

Use of the PFIB made it possible to extend the range of scales investigated and also add additional information regarding the microstructural context of the voids. The X-ray CT imaging allowed a sufficient volume of material to be characterized to produce statistically significant information on the size distribution, void volume fraction and inter-particle distances to understand trends in the voids as a function of depth beneath the fracture surface. The PFIB serial section data is not able to extend to mm-sized volumes like the X-ray CT, but it is a multiscale dataset in its own right and effectively overlaps with the scales captured in X-ray CT. The X-ray CT volume captured effectively resolves the voids 10's of microns in size whilst at the same time capturing carbides 100's of nanometers in size. The PFIB has provided microstructural context of the large voids and made possible the critical observation that each of the voids, including many voids unresolvable from the X-ray CT data, is associated with an inclusion and that the volume of the void scales with the volume of the inclusion raised to the power 3/2, thus emphasizing the importance of the inclusion size distribution.

4. Lab-based nanoscale X-ray CT

As shown in the previous example it is often important to investigate the material at the nanoscale and as discussed in section 2 there are situations where time lapse imaging can be used to help understand processes. One of the major downsides of serial sectioning is that it is destructive and cannot be

utilized for time-lapse studies. However the PFIB can be used to prepare site specific samples suitable for nanoscale X-ray CT (nano-CT) imaging, which is capable of investigating processes over time, in 3D, at the nanoscale. In this exemplar micron-sized specimens are investigated with nanoscale resolution with a temporal resolution of the order of hours.

An experimental procedure to optimize time-lapse imaging using nanoscale X-ray CT has been developed [35]. Bradley et al. explain in detail how the acquisition of both absorption and phase contrast data followed by the effective registration and combination allows for optimum phase identification. In this approach the contrast available through absorption contrast and the edge resolution possible through the phase contrast results is combined to identify the phases with precise interfaces. Here the PFIB has been used for the preparation of the site-specific NanoCT specimens,

4.1 Exemplar: corrosion of AZ31 magnesium alloy

Here, an exemplar of corrosion damage of twin roll cast AZ31 magnesium alloy is presented. There is still a real need to better understand the corrosion of magnesium alloys [36] as this is one of the principal obstacles to its uptake in many engineering and aesthetic applications. Twin-roll casting offers a route to directly produce magnesium sheet in a cost effective way. In this study the propagation of the corrosion in this alloy is investigated to better understand it's interaction with the microstructure.

A pillar of magnesium with dimensions 48 × 50 × 70 μm, was prepared from the middle of a twin roll cast section using mechanical grinding to produce a matchstick of material with dimensions of 2 x 2 x 10 mm^3, but with a sharp point < 500 μm across at one end. The sharpened point was prepared to its final dimensions using a FEI Helios PFIB. The microstructure consists of large mm-sized dendrites. The sample was subsequently immersed in 0.1 M NaCl solution, with the sample removed from the solution for X-ray imaging after cumulative exposure times of 0, 0.5 and 2 hours. Nano-CT was carried out using a Zeiss Xradia Ultra 810 system operated at 5.5 kV. 701 projections were collected with an exposure time of 60 s. Data was collected for a 65 μm field of view with a voxel size of 60 nm. An absorption contrast and phase contrast scan was acquired at each time step. The orientation of the samples was tracked between subsequent scans, and care was taken to ensure registration of the data recorded at the different time steps.

Figure 7(a) shows the time lapse sequence as a 3D rendering, while figures 7(b) and 7(c) show virtual cross sections through the volume at the positions shown by the red and blue lines respectively. The development of corrosion product is clear (seen as darker surface regions) as the surface has developed significant topography; this is quantified by the colour map on the volume surface where the depth of corrosion is shown as the different colours. Here, the depth of corrosion is presented as the difference with respect to the previous time step and not the cumulative total. In this way it is possible to more easily see if corrosion of certain regions has stopped, slowed or accelerated between each immersion step. The dendritic structure of the alloy is clearly visible from the virtual cross sections and bright, high atomic number, particles can be seen decorating the inter-dendritic regions.

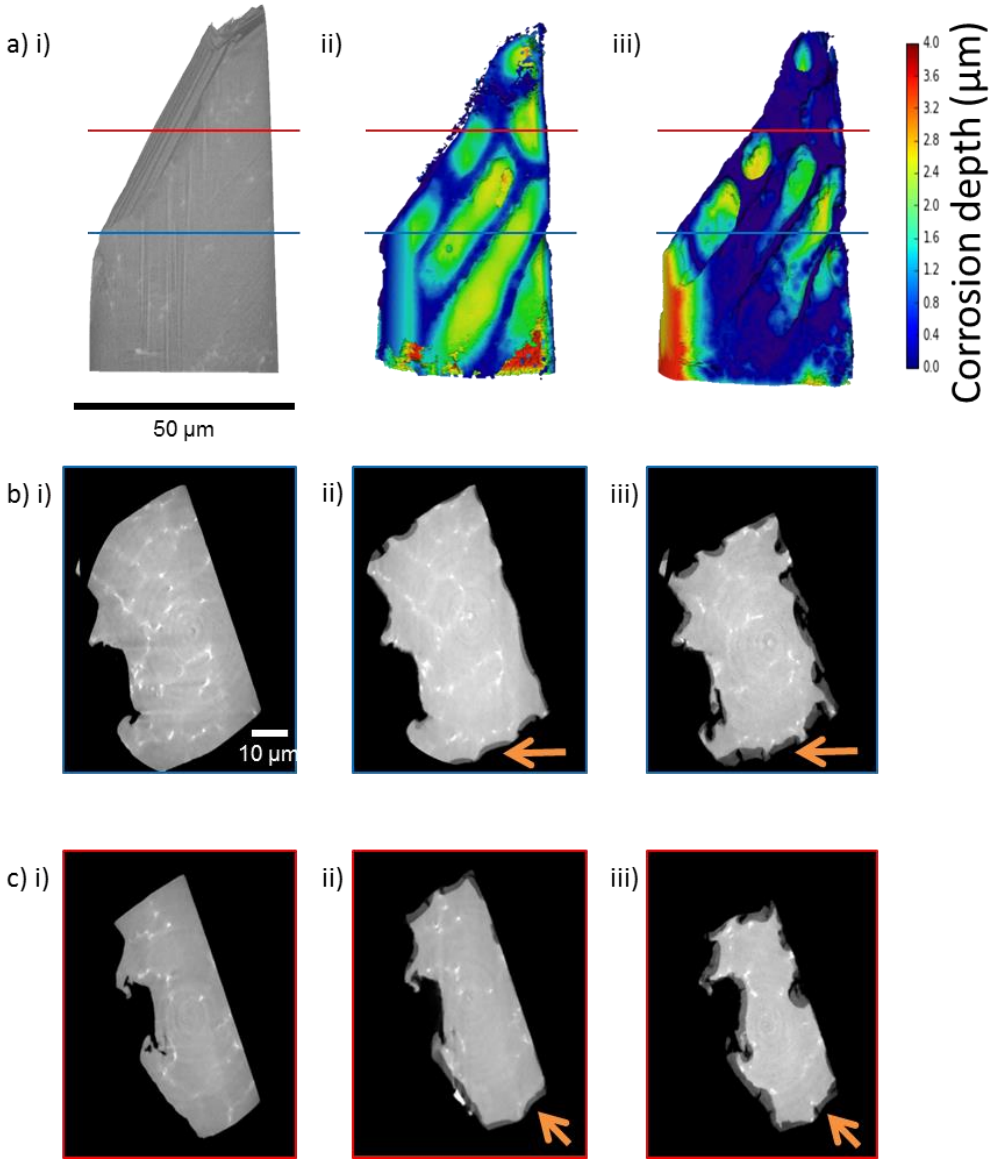

Figure 7 a) shows a volume rendering of the surface of the reconstructed nanoCT data, the red and blue lines indicate the position of virtual slices shown in b) and c). i), ii) and iii) present the same sample after two sequential immersion steps. In a) ii) and iii) the surface is coloured to show the depth of material lost since the previous scan. In b) and c) the same virtual slice is shown for the different time steps, Considerable corrosive attack can be seen, the orange arrow acts as a point of reference.

After 2 hours of exposure the corroded sample was transferred to the FIB-SEM for further analysis. Figure 8(a) shows the surface of the specimen, after being minimally polished using the PFIB (at 30 kV and with a current of 15 nA) to remove the surface topography and corrosion product to allow chemical mapping using EDX (see figures 8b) and 8c). Comparing figure 8(a) with (b) and (c) it is clear to see the correlation and confirm that the interdendritic regions have segregated particles that are Al and Mn rich, although it does appear that some of these are different particles, as the chemical distributions are slightly different. One of these interdendritic regions (from the same sample but without correlation) was analyzed in more detail using STEM-EDS (see figure 8d and 8e). From this it was possible to further understand the complexity of these sites and confirm that the interdendritic

regions are rich in Al and Zn, as expected. In addition, different phase particles are also revealed in these regions as Al and Mn rich particles (which appear bright red and have a feather-like morphology) and also Mg and Si rich particles (which appear bright blue and have a cubic morphology).

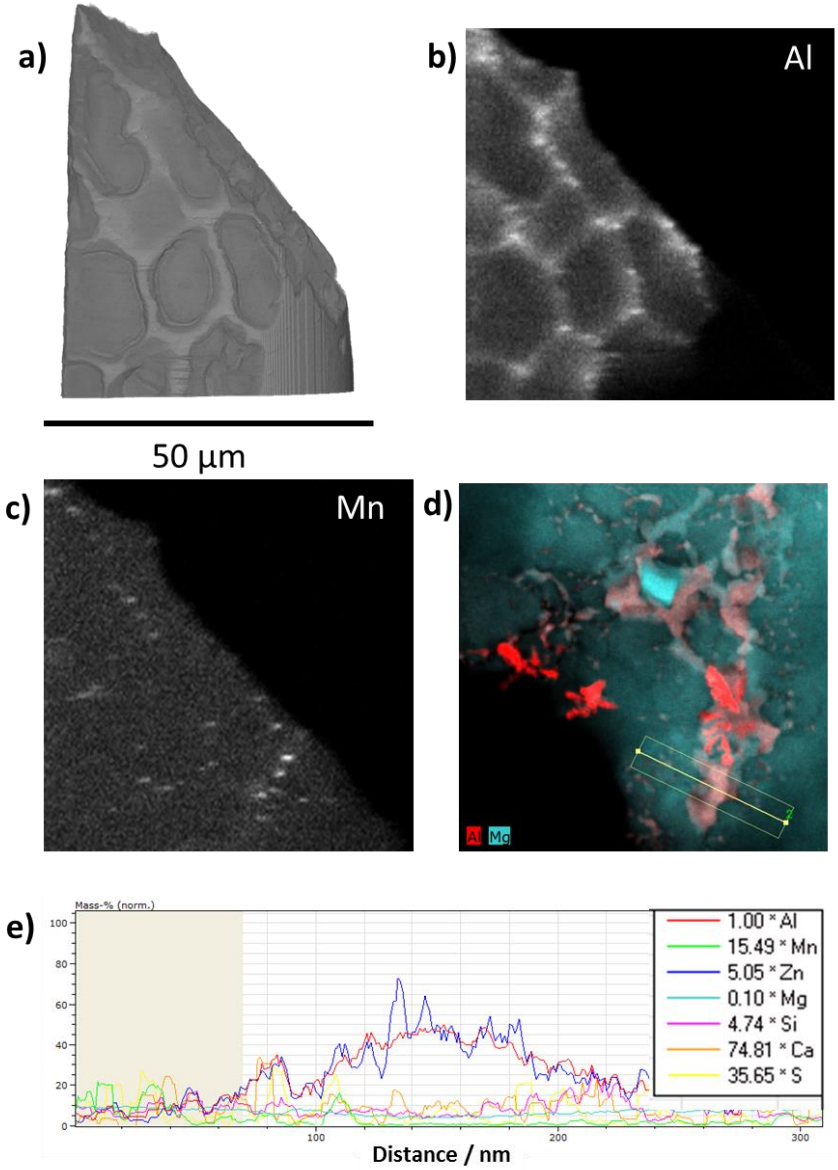

Figure 8 a) shows the surface rendering of the reconstructed nanoCT data after the final corrosion step. b) and c) show EDS maps highlighting Al and Mn respectively. In both cases enrichment appears along the interdendritic regions but there is not a one-to-one correlation of the enriched Al and Mn regions. d) a STEM-EDS spectrum map from one of the interdendritic regions highlighting Al in red and Mg in Cyan the position of a line trace is shown in yellow with the elements present along the length presented in e).

It is clear that the corrosion progresses along the dendrite arms, which are relatively Mg rich [37]. Progress is arrested when the corrosion front reaches the interdendritic regions and is due to the enrichment of the Al and Zn in these regions, although STEM-EDS data shows that the interdendritic region is quite complex with multiple phases all in close proximity. Work is continuing to understand

the role of the multiple phases on the initiation and propagation of the corrosion, which is currently believed to be controlled by small impurity particles.

5. Conclusions

There is a clear desire to investigate and understand many materials systems across multiple time and length scales. To achieve this multiple instruments need to be effectively linked together as no single instrument can provide all of the required functionality. Correlative tomography describes a workflow where regions of interest are successfully targeted to build up a multiscale and multi-layered picture of a sample. The acquired information also has to be effectively connected for an analysis that makes best use of the multiple datasets, typically involving the accurate registration of the datasets. The techniques and exemplars presented in this paper outline a number of complementary approaches, each including different aspects of correlation and different scales of information, which could also be connected in a single study if desirable. In each case the intention is to identify the key time and/or length scales of the process/feature/property so that it can be better understood.

6. Acknowledgements

PJW is grateful for funding through a European Research Council Advanced Grant 695638 (CORREL-CT). The authors would like to acknowledge EPSRC funding for the Henry Moseley X-ray Imaging Facility under grants EP/M010619, EP/K004530, EP/F007906, EP/F028431.**7.** HEFCE funding established the Multidisciplinary Characterization Facility and we are grateful for funding from UK Research Partnership Investment Funding (UKRPIF) Manchester RPIF Round 2. Research support for the work on AA5083-H131 has been provided by the Office of Naval Research thorough ONR-N00014-11-1-0406 (William Mullins), ONR-N00012-14-1-0593 (Airan Perez) and ONR-N00014-15-1-2445 (William Mullins). Additional support has been provided by the Arthur P. Armington Professorship (JJL). Supply of materials was from Alcoa Technical Center.

References

[1] Burnett T L, McDonald S A, Gholinia A, Geurts R, Janus M, Slater T, Haigh S J, Ornek C, Almuaili F, Engelberg D L, Thompson G E and Withers P J 2014 Correlative Tomography *Scientific Reports* **4** 4711

[2] Burnett T L, Kelley R,Winiarski B, Contreras L, Daly M, Gholinia A, Burke M G andWithers P J 2016 Large Volume Serial Sectioning Tomography by Xe Plasma FIB Dual Beam Microscopy *Ultramicroscopy* **161** 119-129

[3] Maire E and Withers P J 2014 Quantitative X-ray tomography *Int. Mater. Rev* **59** 1 1–43

[4] Uchic M D, Holzer L, Inkson B J, Principe E L and Munroe P 2007 Three-Dimensional Microstructural Characterization Using Focused Ion Beam Tomography *MRS Bulletin* **32** (05) 408-416

[5] Thompson G, Hashimoto T, Zhong XL, Curioni M, Zhou X, Skeldon P, Withers P J, Carr J A and Monteith A G 2013 Revealing the three dimensional internal structure of aluminium alloys *Surface and Interface Analysis* **45**(10) 1536–1542

[6] Kübel C,Voigt A, Schoenmakers R, Otten M, Su D, Lee T C, Carlsson A, Bradley J 'Recent Advances in Electron Tomography: TEM and HAADF-STEM Tomography for Materials Science and Semiconductor Applications' Microscopy and Microanalysis, 11, Issue 05, 2005, pp 378-400

[7] Blavettea, D., Duguay, S., Atom probe tomography in nanoelectronics. European Physical Journal - Applied Physics, 2014. 68(1): p. 10101-p1-12

[8] Spowart J 2006 Automated serial sectioning for 3-D analysis of microstructures *Scripta Mater*. **55**(1) 5-10

[9] Winiarski B, Gholinia A, Mingard K, Gee M, Thompson G E and Withers P J 2017 Broad ion beam serial section tomography *Ultramicroscopy* **172** 52–64

[10] Groeber M, Haley B K, Uchic M D, Dimiduk D M, Ghosh S 2006 3D reconstruction and

characterization of polycrystalline microstructures using a FIB-SEM system *Mater Charact* **57**(4-5) 259-273

[11] Hashimoto T, Thompson G E, Zhou X and Withers P J 2016 3D imaging by serial block face scanning electron microscopy for materials science using ultramicrotomy *Ultramicroscopy* **163** 6-18

[12] van Driel L F, Valentijn J A, Valentijn K M, Koning R I and Koster A J 2009 Tools for correlative cryo-fluorescence microscopy and cryo-electron tomography applied to whole mitochondria in human endothelial cells *Eur. J. Cell Biol.* **88** 669–684

[13] Handschuh S, Baeumler N, Schwaha T and Ruthensteiner B A 2013 Correlative approach for combining microCT, light and transmission electron microscopy in a single 3D scenario *Front. Zoo.* **10** 44

[14] Caplan J, Niethammer M, Taylor R M and Czymmek K J 2011 The power of correlative microscopy: multi-modal, multi-scale, multi-dimensional *Curr. Op. Struc. Biol.* **21** 686–69

[15] Robinson B J, Giusca C E, Gonzalez Y T, Kay N D, Kazakova O and Kolosov O V 2015 Structural, optical and electrostatic properties of single and fewlayers MoS2: effect of substrate 2D Mater. 2 015005

[16] Stock S R 2009 MicroComputed Tomography: Methodology and Applications, (CRC Press, Boca Raton, FL, USA)

[17] Herbig M. et al. 2011 3-D growth of a short fatigue crack within a polycrystalline microstructure studied using combined diffraction and phase-contrast X-ray tomography *Acta Mat*. **59** 590–601

[18] Maire E, Owen A, Buffiere J Y and Withers P J 2001 A synchrotron X-ray study of a Ti/SiCf composite during in situ straining *Acta Mater*. **49**(1) 153-163

[19] Qian L, Toda H, Uesugi K, Kobayashi T, Ohgaki T and M. Kobayashi 2005 Application of synchrotron x-ray microtomography to investigate ductile fracture in Al alloys *Appl Phys Lett* **87** 241907

[20] King A, Johnson G, Engelberg D L, Marrow T J and Ludwig W 2008 Observation of Intergranular Stress Corrosion Cracking in a Grain-Mapped Polysrystal *Science* **321** 382–5

[21] Robinson J B, Darr J A, Eastwood D S, Hinds G, Lee P D, Shearing P R, Taiwo O O and Brett D J L 2014 Non-uniform temperature distribution in Li-ion batteries during discharge–a combined thermal imaging, X-ray micro-tomography and electrochemical impedance approach Journal of Power Sources Volume 252, 15 April 2014, pp 51-57

[22] J R. A. Godinho, K M. Gerke, A G. Stack, and P D. Lee The dynamic nature of crystal growth in pores, Sci Rep. 2016; 6: 33086

[23] Lowe, T., Garwood, RJ, Simonsen, TJ, Bradley, RS, Withers, PJ, Metamorphosis revealed time-lapse three dimensional imaging inside a living chrysalis. Journal of the Royal Society Interface, 2013. 10(84)

[24] R Mokso, D A. Schwyn, S M. Walker, M Doube, M Wicklein, T Müller, M Stampanoni, G K. Taylor & H G. Krapp, Four-dimensional in vivo X-ray microscopy with projection-guided gating, Scientific Reports 5, Article number: 8727 (2015)

[25] NJH Holroyd, TL Burnett, M Seifi, JJ Lewandowski, Improved understanding of environment-induced cracking (EIC) of sensitized 5XXX series aluminium alloys, 2017, Materials Science and Engineering: A, Volume 682, Pp. 613-62

[26] M. Seifi, N.J.H. Holroyd, J.J. Lewandowski, Deformation rate and sensitization effects on environmentally assisted cracking Al-Mg naval alloys, Corrosion 72 (2016) 264–283

[27] M Daly, TL Burnett, EJ Pickering, OCG Tuck, F Léonard, R Kelley, PJ Withers, AH Sherry, A multi-scale correlative investigation of ductile fracture, 2017, Acta Materialia Volume 130, Pp. 56-68

[28] T L Burnett, B Winiarski, R Kelley, X L Zhong, I N Boona, D W McComb, K Mani, M G Burke, P J Withers, Xe+ Plasma FIB: 3D Microstructures from Nanometers to Hundreds of Micrometers, 2016, Microscopy Today Volume 24 Issue 03 Pp. 32-39

[29] Jiruše, J., Hrnčiř, T, Lopour, F, Zadražil, M, Delobbe, A, and Salord, O, Combined plasma FIB-SEM. Microsc. Microanal., 2012. 18 ((Suppl 2)): p. 652-653
[30] **http://symmetry.oxford-instruments.com/**
[31] Yu-Hui Chen, S Un Park, D Wei, G Newstadt, M Jacksona, J P. Simmons, M De Graef A O. Hero, A Dictionary Approach to EBSD Indexing, 2015, Microscopy and Microanalysis Volume 21 Iss: 03 Pp. 739-752
[32] P G Callahan, M De Graef, Dynamical electron backscatter diffraction patterns. Part I: Pattern simulations, 2013, Microscopy and Microanalysis Volume 19 Issue 05 Pp 1255-1265
[33] ASTM Standard Specication for Quenched and Tempered Vacuum-treated Cabon and Alloy Steel Forgings for Pressure Vessel ComponentsA508A/A508M (2004)
[34] ESIS TC1 Subcommittee on Fracture Mechanics Testing Standards, ESIS Procedure for Determining the Fracture Behaviour of Materials ESIS P2-92, Tech. rep., European Structural Integrity Society (1992)
[35] R.S. Bradley, Y. Liu, T.L. Burnett, X. Zhou, S.B. Lyon, P.J. Withers, A. Gholinia, T. Hashimoto, D. Graham, S.R. Gibbon, B. Hornberger, Time-lapse lab-based x-ray nano-CT study of corrosion damage, 2017, Volume 267, Issue 1, Pp. 98–106
[36] Esmaily M, Svensson J E, Fajardo S, Birbilis N, Frankel G S, Virtanen S, Arrabal R, Thomas S and Johansson L G 2017 Fundamentals and advances in magnesium alloy corrosion *Prog Mater Sci* **89** (2017) 92–193
[37] Pawar S, Slater T J A, Burnett T L, Zhou X, Scamans G M, Fan Z, Thompson G E and Withers P J 2017 Crystallographic effects on the corrosion of twin roll cast AZ31 Mg alloy sheet *Acta Mater.* **133** 90-99